DAYTIME ADAPTIVE OPTICS FOR DEEP SPACE OPTICAL COMMUNICATIONS

Session C2

[§]K. Wilson, M. Troy, M. Srinivasan, B. Platt, V. Vilnrotter, M. Wright, V. Garkanian, H. Hemmati

The deep space optical communications subsystem offers a higher bandwidth communications link in smaller size, lower mass, and lower power consumption subsystem than does RF. To demonstrate the benefit of this technology to deep space communications NASA plans to launch an optical telecommunications package on the 2009 Mars Telecommunications Orbiter spacecraft. Current performance goals are 30-Mbps from opposition, and 1-Mbps near conjunction (~3 degrees Sun-Earth-Probe angle). Yet, near conjunction the background noise from the day sky will degrade the performance of the optical link. Spectral and spatial filtering and higher modulation formats can mitigate the effects of background sky. Narrowband spectral filters can result in loss of link margin, and higher modulation formats require higher transmitted peak powers. In contrast, spatial filtering at the receiver has the potential of being lossless while providing the required sky background rejection. Adaptive optics techniques can correct wave front aberrations caused by atmospheric turbulence and enable near-diffraction-limited performance of the receiving telescope. Such performance facilitates spatial filtering, and allows the receiver field-of-view and hence the noise from the sky background to be reduced.

1. INTRODUCTION

The role of adaptive optics in astronomy is well established, and the use of natural and laser guide stars to correct atmosphere-induced wave front aberrations from the source of interest is well developed and used at several astronomical sites around the world. The application of adaptive optics to space-to-ground optical communications, however, is relatively new, and unlike stellar astronomy, the signal source in optical communications is not fixed with respect to the stars but like the planets moves across the star field. The principal application of this technology to deep space optical communications is in improving the signal-to-noise ratio (SNR) of the downlink during daytime reception.

With NASA's new initiative in deep space optical communications [1], JPL is exploring strategies to mitigate the effects of daytime sky background radiation on the optical communications link. Analysis shows that the period of communications outage ranges from 23 days for a Sun-Earth-Probe (SEP) angle exclusion of 3 degrees to approximately 260 days for a SEP exclusion angle of 30 degrees. The 1-m telescope in the newly-built JPL Optical Communications Telescope Laboratory (OCTL) [2] is designed to operate to within 10 degrees of the sun (corresponding to eighty-nine days outage) and will be used to assess strategies to mitigate the effects of sky background on the optical link.

In this paper we discuss the application of adaptive optics (AO) to the deep space link and present our early analytical results that demonstrate the improvement in the optical communications system performance when adaptive optics techniques are implemented in a high background environment. In Section 2 we discuss adaptive optics for deep space optical communications and the wave front correction realizable as a function of actuator density for nominal atmospheric seeing conditions at JPL's Table Mountain Facility. We present a communications analysis and show the SNR improvement realized as a function of actuator density for various communications modulation formats in Section 3, and describe our test bed that we are currently building to validate our theoretical models in Section 4.

§ The authors are affiliated with JPL/CalTech, 4800 Oak Grove Dr. Pasadena CA 91109-8099

2. DAYTIME ADAPTIVE OPTICS

The need of AO in optical communications is during the daytime when the scatter from sky the background into the receiver is high. For the deep space data rates, the technology offers no advantage to nighttime operations of a direct detection link. The advantage of this technology is most evident when pointing close to the sun in poor seeing conditions. Under these conditions, AO can minimize the amount of sky background collected by the detector by concentrating the optical communication signal energy in the focal plane. This is a significantly more difficult goal than that of current astronomical AO systems where the objective is resolution. Here, diffraction limited cores with "modest" Strehl ratios of ~50% at observing wavelengths of 1-2.2 μm, and the ability to point anywhere in the sky are the key goals. In optical communications, the goal is to decrease the total energy in some diameter. We have defined 80% enclosed energy diameter (corresponds to ~1-dB signal loss) as a metric. To appreciate the impact of the 80% enclosed energy metric, it is important to understand, at least heuristically, the structure of AO images. Without any AO correction long exposure image widths are $\sim\lambda/r_0$. As the amount of AO correction increases energy is pulled into a diffraction-limited core, of width λ/D. However, much of the energy is still in the $\sim\lambda/r_0$ halo, in the case of x% Strehl ~100-x% of the energy remains in the halo. This is seen in Figure 2.1.

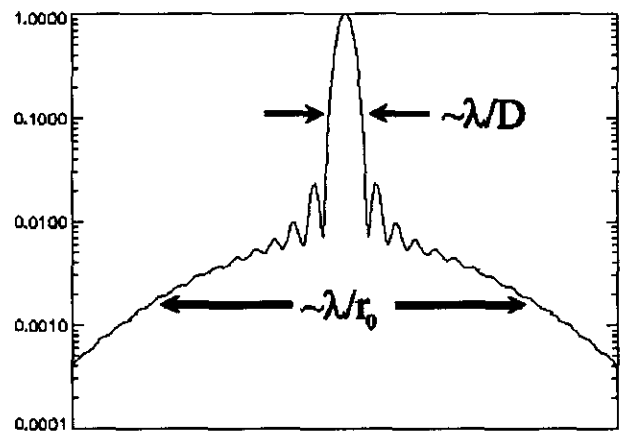

Figure 2.1: One dimensional cut of a pictorial 50% Strehl AO, showing a "diffraction limited" core and a large seeing halo. 50% of the energy remains in the halo of the image.

In fact, if the actuator spacing is 30-cm (at the primary mirror) then spatial frequencies larger than $\sim\lambda$ (2*30cm) or 0.37 arc-seconds (at 1064-nm) cannot be significantly affected by the deformable mirror. As a result, the 80% enclosed energy diameter does not change significantly until the actuator spacing is on the order of r_0.

The above arguments are heuristic. To quantify the improvement in 80% enclosed energy diameter and ultimately the bit error probability, we used two approaches to create simulated AO images; the second as a check against the first. The goal of our simulation was to produce short exposure images that modeled only the AO error term as a function of the number of deformable mirror (DM) actuators used to fit to the atmospheric turbulence. This is also known as atmospheric fitting error. This approach set an upper bound on AO system performance. The images were then analyzed to determine the 80% enclosed energy, the RMS wave front error, and the improvements in bit error rate as a function of number of DM actuators. Several AO systems were simulated, ranging from no actuators (and hence no compensation) to as many as

200 actuators across the pupil diameter. The limiting case of no wave front aberration (no signal distortion) was also determined by computing performance assuming an undistorted "diffraction limited" point spread function.

Images were created by first generating a Kolmogorov phase screen with a 7-cm r_0 at 1064-nm. Next, a portion of the phase screen corresponding to a 1-meter telescope was extracted. In the first approach, a parabolic filter function was created based on the DM actuator spacing to simulate the atmospheric fitting error [3], and the filter applied to the 1-meter phase screen. The phase screen was propagated to the image plane and the final image down sampled to the desired pixel scale.

The second method for simulating the atmospheric fitting error was to instead of filtering the phase screen with a parabolic filter, to remove the first N Zernikes from the phase screen. The actuator spacing was set equal to ~$1.2/\sqrt{N}$-m. The factor of 1.2 was determined by requiring that the long-exposure RMS wave front error match the atmospheric fitting error function, $0.28\left(\frac{d}{r_0}\right)^{\frac{5}{6}}$, where d is the sub-aperture size [4]. Both methods of simulation gave similar results for 80% enclosed energy and bit error rates. For the remainder of this paper we will present only results from the first method of simulation.

Figure 2 shows the short exposure images on a logarithmic scale. As the sub-aperture spacing is decreased the control radius is improved. As predicted above, the 80% enclosed energy begins to improve at a sub-aperture spacing equal to r_0 (7-cm). At a sub-aperture spacing of 3.3-cm, about half of the r_0, a significant improvement of the image is observed. Figure 2.3 plots both the 80% enclosed energy diameter and RMS wave front error as a function of size of sub-aperture or alternatively the number of actuators across a 1-meter pupil. Current AO systems achieve RMS wave front errors on the order of 200 to 250-nm. At this level of correction they are just starting to reduce the spot size of the 80% enclosed energy. In order to reduce the 80% enclosed energy spot size significantly, RMS wave front errors on the order of 50 to 100-nm are required. This implies on the order of 30 actuators across a 1-meter telescope. In the following section the simulated images are used to determine bit error probabilities as a function of sky background and number of AO actuators.

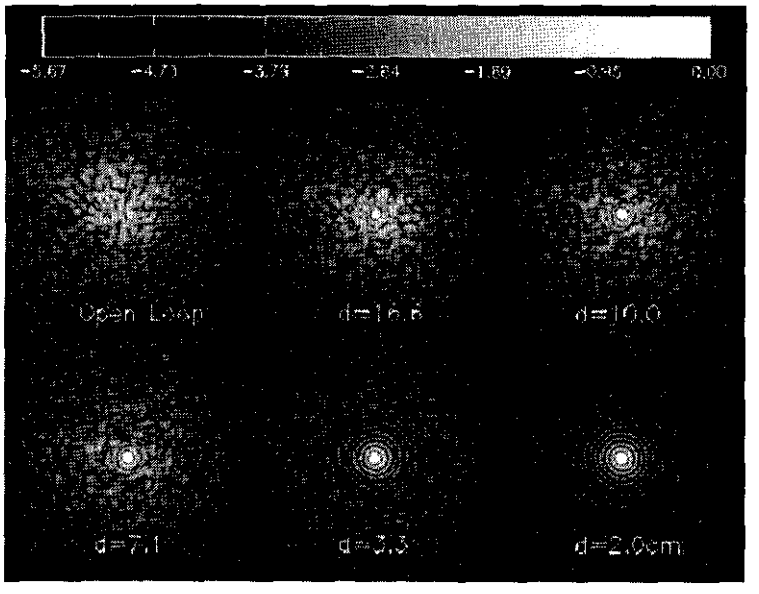

Figure 2.2: Simulated short exposure AO corrected images. The telescope is 1-meter, the images are at 1.064 μm and r_0 is 7-cm at 1.064-μm. Only atmospheric fitting error is modeled, the labels on each image indicated the DM actuators spacing. Each image is 10 arc-seconds on a side and the sampling is λ/(4*D) radians/pixel. The affect of the actuator control radius can be seen as the actuator spacing is decreased.

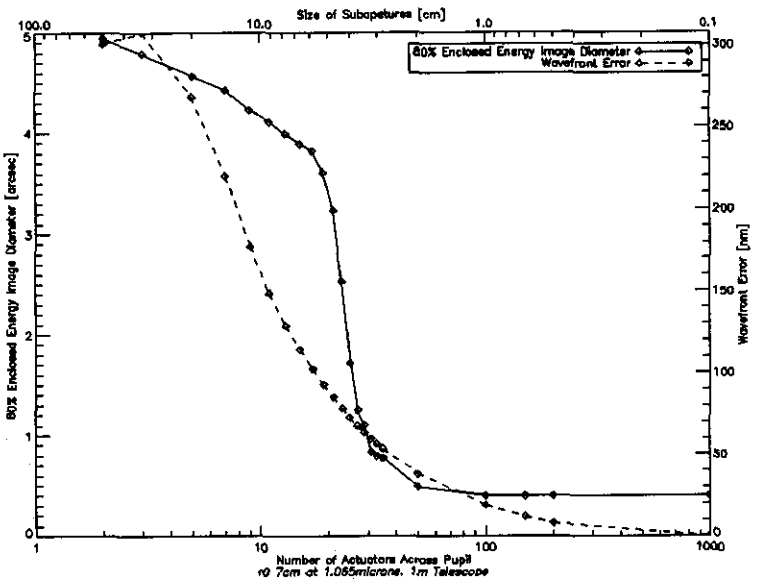

Figure 2.3: Simulated short exposure AO images were used to calculate both the 80% enclosed energy diameter and the wave front error as a function of actuator spacing. To get a significant decrease in the 80% enclosed energy actuator spacings of about 3cm (or $r_0/2$) are required.

3. *COMMUNICATIONS ANALYSIS*

In this section, the performance of adaptive optics-aided direct detection of optical communication signals received through atmospheric turbulence is evaluated. The performance is characterized in terms of the uncoded pulse-position modulation bit error rates as a function of AO complexity, and the corresponding gains of adaptive optics systems are determined over that of nominal reception, i.e., no adaptive optics compensation. Processing algorithms developed in [5] have been applied to this problem. There it was shown that near-optimum performance could be obtained using a relatively simple adaptive "1-0" strategy for processing the outputs of focal-plane detector arrays, instead of the optimal detection strategy that involves the computation and application of logarithmic weights to each detector output. The use of adaptively synthesized single detectors of the correct dimensions with a well-defined geometry (such as square, rectangular, or circular) has also been considered, and it was shown that under certain conditions performance close to the adaptive "1-0" strategy could be approached with a square detector whose dimension (number of detector elements across) was adjusted adaptively to match the signal field distribution in the focal-plane. The implications of this approach for implementation are significant, since the complicated processing of selecting the correct number of possibly disjoint detector elements required both for the optimal and the "1-0" strategies can now be replaced with simpler processing applied to a regular sub-array, or even a single large detector element with appropriate zoom optics to achieve the required spatial adaptation as the size of the point spread function changes due to turbulence. Numerical results originally presented in [5] for both the adaptive "1-0" focal plane array processing approach and the synthesized single detector approach were applied to the adaptive optics problem, and evaluated assuming photon counting detection of Poisson distributed signal and background counts.

The effect of atmospheric turbulence upon the optical signal intensity distribution in the focal plane is twofold. First, small-scale turbulence distorts the diffraction limited point spread function and effectively "spreads" the signal intensity over a larger area than the diffraction limited point spread function. Second, the centroid of the distribution wanders in the focal-plane, the extent of the excursions determined by the outer scale of turbulence [6]. Compensating for this effect requires a larger area

photodetector to capture the required number of signal photons to achieve the desired level of performance. The background radiation intensity is assumed to be uniformly distributed over the focal plane detector, and the larger number of photodetectors containing significant signal energy (or a larger effective detector area) results in proportionally more background photons collected, and hence degraded communications performance. With adaptive optics, however, the wave front aberrations caused by turbulence are compensated to some extent resulting in a concentration of the signal energy into a smaller area in the focal-plane, and an improved discrimination against unwanted background interference.

3.1 PERFORMANCE ANALYSIS

The process of determining communications performance begins with the simulation of the effect of atmospheric turbulence on the focal plane signal distribution through the use of Kolmogorov phase screens [7]. A 1 Angstrom optical filter around a nominal signal wavelength of 1064-nm is included in the model to reduce the background spectral irradiance. The background photon level, which depends upon the spectral radiance of the noise source and the receiver field-of-view, is a key parameter in determining communications performance. Therefore, three different values of spectral radiance were assumed, corresponding to vastly different background conditions and environments. The values of spectral radiance considered were (in units of microwatts per squared centimeter-nanometer-steradian)

- 0.5, corresponding to 3 km altitude daytime clear sky [8]
- 10, corresponding to daytime nominal sea level [8]
- 100, corresponding to sunlight scattering from optics [9]

The conversion of these values into the number of background photons per pulse position modulation (PPM) slot depends upon the photodetector size, the data rate and the PPM order used. As the photodetector size is optimized for the number of actuators used in the AO system, we give background photon levels per diffraction-limited field of view, or "pixel". At a nominal data rate of 10 Mbps, the average numbers of background counts per PPM slot, per diffraction limited pixel are: 5.23×10^{-5}, 1.05×10^{-3}, and 1.05×10^{-2} for 256-PPM for the three different spectral radiance values respectively. For 64-PPM, the values are 1.57×10^{-4}, 3.14×10^{-3}, and 3.14×10^{-2}, and for 16-PPM the values are 4.19×10^{-4}, 8.37×10^{-3}, and 8.37×10^{-2}. The actual average number of background photons per slot is then calculated from these numbers by summing over the number of diffraction limited pixels in the detector, which varies from over one thousand for no AO to one for the most complex AO systems. We further assumed direct photon counting detection with Poisson output statistics for both the signal fields and the background radiation: the latter case can be justified by the assumption of multimode background fields, as described in [5].

Two methods of photodetector signal processing were considered: one using an array of detectors and the other usingj ust a single large detector. In [5], it was shown that the deleterious effect of atmospheric turbulence could be mitigated by using an array of photodetectors in the focal plane, and then processing the outputs of those detector elements to minimize the bit error rate. As shown in [5], the probability of correct detection for PPM is just the probability that the log-likelihood function $\Lambda(T)$ associated with the transmitted symbol exceeds all other log-likelihood functions. Thus, when the q-th PPM symbol is sent, a correct decision is made if the log-likelihood function for the q-th hypothesis exceeds the log likelihood function for all other(i ncorrect) hypotheses: $\Lambda_q(T) > \Lambda_i(T)$ for all $i \neq q$. The log-likelihood function can be expressed as

$$\Lambda_i(T) = \sum_{m=1}^{K} \sum_{n=1}^{L} u_{mn} \; N_{mn}^{(i)} \quad ,$$

where u_{mn} is a logarithmic function as defined in [5]. In this form, we can see that the log likelihood function is composed of sums of a random integer number of logarithmic weights from each detector element. The optimum PPM detection is thus determined by calculating a logarithmically weighted sum of detector outputs for each hypothesized signal slot and picking the PPM symbol corresponding to the

maximum sum. However, the analysis in [5] suggests that detectors observing much more background than signal do not contribute significantly to the error probability, since the output of these detector elements are multiplied by weights that are close to zero. This observation leads to a simpler but sub-optimum decoder concept. Computationally, one lists the detector elements starting with the one containing the most signal energy, followed by every other detector ordered according to decreasing signal energy, then computes the probability of error for the first detector element plus background, next one forms the sum of signal energies from the first two detector elements (plus background for two detector elements). This process is iterated until the minimum error probability is reached. Each subset of detectors may be considered a single detector with no weighting applied. This is to account for variations in the signal distribution over the detector elements included in that set. The set of detector elements that achieves the minimum probability of error is the best "1-0" detector matched to the signal intensity distribution.

In effect, this strategy is equivalent to partitioning the logarithmic weights into two classes. Large weights that are assigned the value one, and small weights that are assigned the value zero. As shown in [5], this simple partitioning achieves near-optimum performance in low to moderate background environments, but with reduced decoder complexity. Even in high background environments its performance is only a few tenths of a dB worse than the optimally weighted array. This "1-0"array detection algorithm is the method used to process the data in this paper.

As an alternative to processing the numerous detector outputs, one may choose to simply use a single large detector that collects most of the signal energy in the focal plane. The size of this single detector must vary with the signal distribution in the focal plane in order to most effectively capture the signal energy and reject background. This variablesi ze single detector may therefore be viewed as a detector array constrained in its geometry, but may be implemented through the use of an iris in front of a single large detector in the focal plane. Here, we assume the use of a single square detector of a size that minimizes the probability of bit error and is centered at the maximum signal intensity point in the focal plane.

The received symbol is decoded correctly if the sum of weights from all detector elements over the signal-slot exceeds the sum of weights from every other (non-signal) slot. The probability of a symbol error is simply one minus the probability of correct detection, or $P_M(E) = 1 - P_M(C)$. When the array consists of a single detector, the weights can be set to one, and the probabilities are then governed by the Poisson density defined over the integers.

For both the adaptive "1-0" strategy and the structured single "best" detector described above, the probability of correct detection can be obtained by assuming constant signal and background intensities over each time-slot, yielding the conditional probabilities for the signal-plus-background and background slots, respectively, as

$$p_q(k \mid H_q) = \frac{(\lambda_s\tau + \lambda_b\tau)^k}{k!} e^{-(\lambda_s\tau+\lambda_b\tau)} \quad \text{and} \quad p_i(k \mid H_q) = \frac{(\lambda_b\tau)^k}{k!} e^{-\lambda_b\tau}$$

where $\lambda_s\tau$ and $\lambda_b\tau$ are the average signal and background counts over τ-second signal and background slots, respectively, and over the detector array or single detector area. The probability of correct detection can be determined using these Poisson densities, as:

$$P_M(C) = \left\{ \sum_{r=0}^{M-1} \left(\frac{1}{r+1}\right) \binom{M-1}{r} \sum_{k=1}^{\infty} \frac{(\lambda_s\tau + \lambda_b\tau)^k}{k!} e^{-(\lambda_s\tau+\lambda_b\tau)} \left[\frac{(\lambda_b\tau)^k}{k!} e^{-\lambda_b\tau}\right]^r \left[\sum_{j=0}^{k-1} \frac{(\lambda_b\tau)^j}{j!} e^{-\lambda_b\tau}\right]^{M-1-r} \right\}$$

$$+ M^{-1} e^{-(\lambda_s + M\lambda_b)\tau} \tag{18}$$

This, in turn, yields the probability of error as $P_M(E) = 1 - P_M(C)$. The resulting error probability was then evaluated to determine the performance of the AO system under various operating conditions of interest.

3.2 RESULTS

Figure 3.2.1 shows the uncoded bit error probability as a function of the total number of absorbed signal photons per signal pulse, for 64-PPM with background level as specified by the smallest spectral radiance value given earlier in [5]. The curves are shown for selected numbers of actuators n across the pupil to correct wave front error: $n = 0$, $n = 9$, $n = 31$, and for the case of no wave front error. In addition, results are given for both the single and array-detector processing schemes. We see from this plot that the difference between the performance of the single detector and the array detector is less for the higher actuator density AO systems. For example, at a bit error rate of 10^{-6} the performance difference between the single detector and the array is about 0.3 dB for the $n = 0$ case, i.e. no AO. This difference is reduced to 0.002 dB when the wave front distortions are completely compensated i.e., no wave front error. This reduction is due to the fact that the improved wave front correction allows for improved spatial filtering and hence a reduction in background light incident on the single detector, allowing it to perform as well as the array. We also see that the $n = 9$ AO system only improves the performance of the uncompensated $n = 0$ system by about a tenth of a dB at 10^{-2} bit error rate (BER), whereas the $n = 31$ AO system results in an improvement of more than 1 dB, and about 0.5 dB short of the limiting performance (at 10^{-2} BER) corresponding to no wave front error.

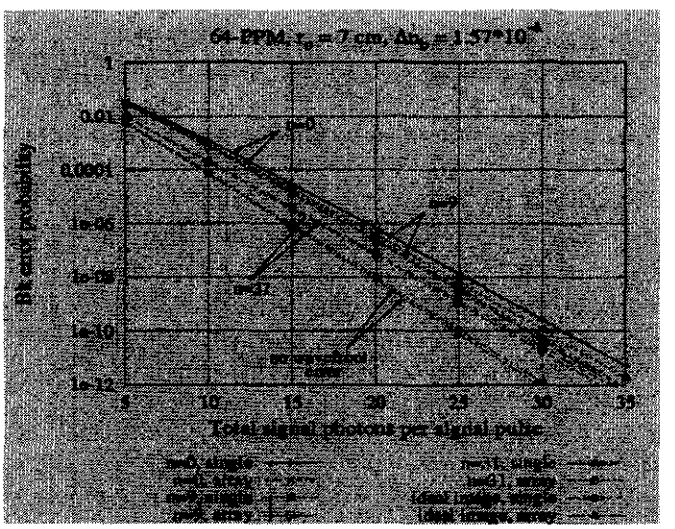

Figure 3.2.1: Uncoded bit error probability as a function of the total number of absorbed signal photons per signal pulse, for 64-PPM for 1.57x 10^{-4} background counts per slot.

Figure 3.2.2 shows the same bit error rates as Figure 3.2.1, but now as a function of the number of actuators across the pupil, for three values of total number of signal photons per pulse of 5, 10 and 20. A vertical line is drawn at a value of 31 actuators across, denoting what may be currently implemented in a one-meter telescope. This figure again shows how close the array and single detector performances are, as well as the degree of improvement afforded by more complex AO systems.

Figures 3.2.3 and 3.2.4 show the 64-PPM results, now using spectral radiance case given in reference 9. Again a vertical line is drawn at a value of 31 actuators across. We see that with the larger amount of background, the improvement in performance given by more actuators is much greater, and that

the difference between the single detector and the detector array is also greater, as the improved background rejection capability of the array processing is of more value in this case. We see here that at 10^{-2} BER, the n=31 AO system improves performance by about 4.5 dB.

Figures 3.2.5, 3.2.6, and 3.2.7 show the performance gain values at 10^{-2} uncoded BER for the three background cases and 16-PPM, 64-PPM, and 256-PPM modulation formats, respectively,. Note that while improvements as great as 3-6 dB are indicated for the high-background case. This would occur if direct sunlight were to strike the receiver optics, resulting in a great deal of scattered light from surface irregularities and dust. However, as indicated by the first bar in the Figures, improvements of 1-2 dB appear feasible under actual operating conditions when the spacecraft is close to the sun, and gains of 2-3 dB may be realized under unusual circumstances such as low-elevation reception close to the sun, or when looking through highly scattering light clouds resulting in exceptionally great levels of background photons entering the receiver.

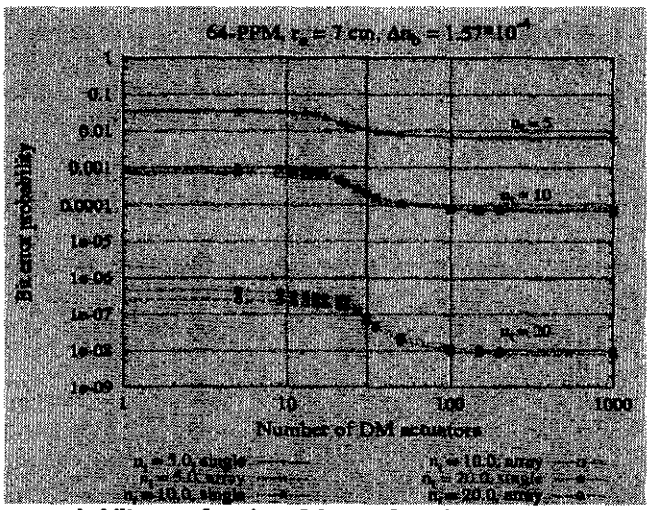

Figure 3.2.2: Bit error probability as a function of the number of actuators across the pupil, for three values of *total number of signal photons per pulse* of 5, 10 and 20 and 1.57x 10^{-4} background counts per slot.

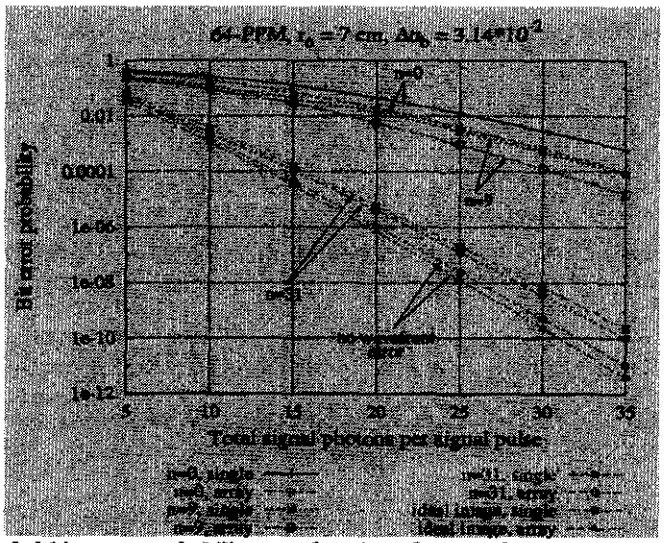

Figure 3.2.3: Uncoded bit error probability as a function of the total number of absorbed signal photons per signal pulse, for 64-PPM for 3.14x 10^{-2} background counts per slot.

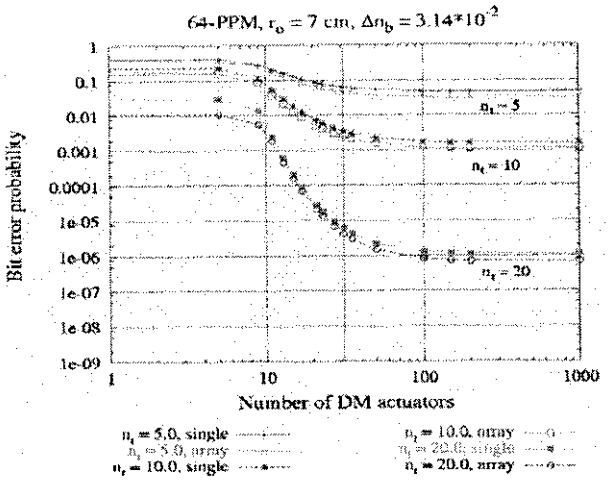

Figure 3.2.4: Bit error probability as a function of the number of actuators across the pupil, for three values of total number of signal photons per pulse of 5, 10 and 20 and 3.14 x 10^{-2} background counts per slot.

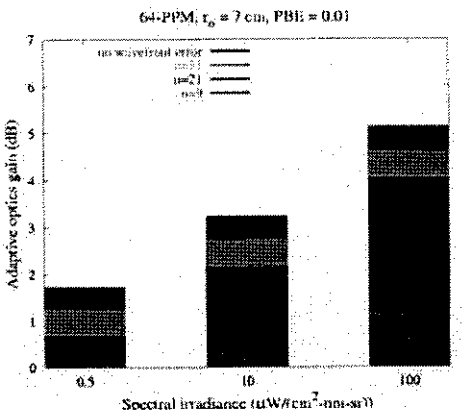

Figure 3.2.5: Theoretical performance gain for 16–PPM for the three levels of background noise. Gains shown for adaptive optics system with n^2 (n=9,21,31) actuators across a 1-m aperture.

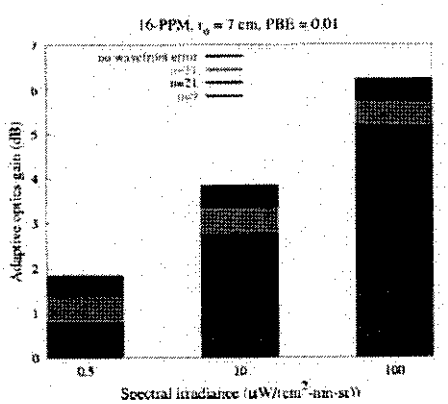

Figure 3.2.6: Theoretical performance gain for 64–PPM for the three levels of background noise. Gains shown for adaptive optics system with n^2 (n=9,21,31) actuators across a 1-m aperture.

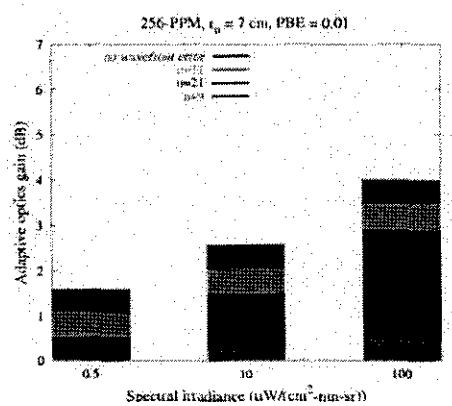

Figure 3.2.7: Theoretical performance gain for 256–PPM for the three levels of background noise. Gains shown for adaptive optics system with n^2 (n=9,21,31) actuators across a 1-m aperture.

4. ADAPTIVE OPTICS TEST BED

Figure 4.1 is a schematic of the AO test bed that has been designed to demonstrate and validate the performance improvement achieved by adaptive optics in deep space optical communications. The test bed design is based on the results of Section 3.1. Table 4.1 is an itemized list of the components. The 77-mm DM defines the size both the AO reference beam and the laser communications beam. The atmospheric turbulence generator (ATG) and the DM are located in the collimated space between the two off-axis-parabolas (OAP). The turbulence generator consists of a perforated plate placed over a heater, and is designed to produce phase structure functions that have Fried parameters (r_0) ranging from sub-DM actuator spacing to several times the DM actuator spacing "d". The AO scaling parameter (d/r_0) is a design parameter in the test bed. The metric for the AO tests will be the bit error rate improvement in the laser communications signal.

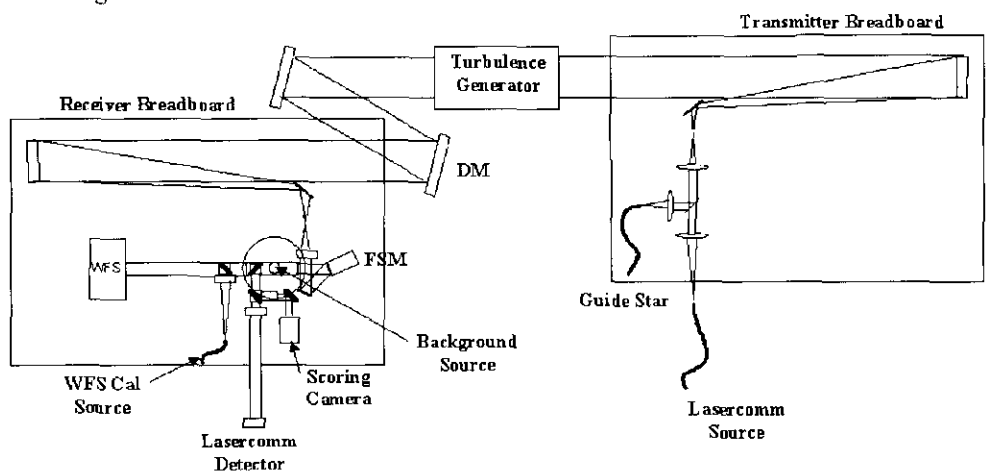

Figure 4.1: Schematic of Lasercomm AO test bed

The optical sources are a beacon laser consisting of single mode fiber coupled 633-nm diode laser that serves as a guidestar simulator or a calibration source for the wave front sensor (WFS) camera, and a single mode 1060-nm

fiber coupled diode laser transmitter for the communications link. The transmitter laser is temperature controlled for wavelength and power stability, and can be operated at 200 MHz modulation rates. The laser electronics support on-off-keying (OOK) and PPM modulation formats. Currently, a bit error rate tester is used to generate the OOK modulation format as an input to the laser driver. The PPM format is generated using a custom-developed FPGA (Field Programmable Gate Array) circuit. The laser communication detector is an IR enhanced Si:APD (silicon avalanche photo diode) detector. Silicon detectors were chosen over InGaAs due to their low noise and large area at our operating bandwidth. We anticipate that the eventual deep-space receiver would also use Si:APD detectors or Si Geiger mode detectors.

Table 4.1: Description of components in the Lasercomm AO test bed.

Component	Function	Parameters
Deformable Mirror	Correct aberrations caused by the ATG.	97 actuators on 7mm centers, 4.8μm mechanical stroke, 2μm inter actuator stroke, 4KHz freq. response.
Fast Steering Mirror	Correct tilt/tip errors in the beam caused by the ATG.	2.5-cm diameter, +/- 1mrad travel, 0.05μrad resolution, 2 axis, 1KHz freq response.
Wavefront Control System	Measure aberrations and tilt errors caused by the ATG, process the signals and send control signals to the DM.	Hartmann WFS, 16x16 sub-apertures, 2K fps,
Laser Comm Source	Simulate a laser comm signal from a point source at infinity.	1064-nm laser diode, 15 mW, 100 MHz, single mode fiber coupled
Adaptive Optics Reference Source	Simulates a star, laser guide star or laser beacon.	633-nm laser diode, 7 mW, single mode fiber, cw
Laser Comm Detector	Detects the lasercomm signal.	200, 500 μm diameter IR enhanced Si APD > 100 MHz
Scoring Camera	Measures the intensity profile of the beam on the laser comm. detector.	Hitachi near IR CCD, KP-M2R, 768x494 pixels, 8.4x9.8μm pixel size, RS-170 video out.
Background Radiation Source	Simulates sky background radiation.	15-cm diameter 600 to 900nm spectral range, 46μW/(cm^2-steradian-nm) at 1040nm output, traceable to National Institute of Standards and Technology (NIST), LS-65-8D Rev. B.
Atmospheric Turbulence Generator	Simulates atmospheric turbulence of both sources.	r_0 = 3.5 to 14mm, 77mm clear air turbulence generated by differentially heating air.

The receiving telescope after the second OAP reduces the beam to 15-mm before becoming incident on the fast steering mirror (FSM) and the background source. The laser communications beam is split off to the laser communications detector and the scoring camera. The scoring camera presents an image of the laser beam that is incident on the laser communications detector. A zoom lens is used to change the size of the diffraction pattern on the laser comm. detector. The AO reference beam is incident on a Shack-Hartmann WFS that measures the atmospheric tilt and aberrations on the optical beam. The tilt error signal is sent to the FSM controller and the higher order wavefront error signals are sent to the DM controller.

Calibrated levels of background radiation at the 1064-nm wavelength will be introduced into the optical path using an integrating sphere. The sphere can generate background levels in the range of 0.5 to 10 μW/(cm^2-steradian-nm). The background level will be appropriately attenuated so that the background levels at the detector are consistent with those analyzed in Section 3. The control parameters of the tests are r_0, the size of diffraction pattern on the laser communications detector, and the level of background

radiation. The BER of the optical link will be characterized as a function of d/r_0 for various background light levels.

5. SUMMARY

We have described JPL's research effort in adaptive optics to mitigate the effects of background noise on the daytime deep space optical communications link. Results show that depending on modulation format and background levels, as much as 6-dB improvement in link margin can be realized in a high background environment. We have described the design of an AO testbed that will be used to validate our models.

6. ACKNOWLEDGEMENTS

The research described in this paper was carried out at the Jet Propulsion Laboratory, California Institute of Technology under a contract with the National Aeronautics and Space Administration

The authors would like to acknowledge the support of Drs. J. Yuen and F. Pollara of JPL for their contributions and support of this work.

7. REFERENCES

1. B. Edwards, et al. "Overview of the Mars Laser Communications demonstration Project" to be published American Institute of Aeronautics and Astronautics Space 2003, September 25, 2003.
2. K. Wilson, "Planned Operations for the JPL Optical Communications Telescope Laboratory (OCTL), Invited Paper, CRL International Symposium on Light Propagation and Sensing Technologies for Future Applications, Tokyo, March 2002.
3. A. Sivaramakrishnan, C. D. Koresko, R. B. Makidon, T. Berkefeld, M. J. Kuchner, "Ground-based coronagraphy with high-order adaptive optics," The Astrophysical Journal, pg.397, Volume 552, No. 1 Part 1, May 2001.
4. J. H. Hardy, *Adaptive Optics for Astronomical Telescopes*, pg. 342. Oxford University Press, New York, 1st ed., 1998.
5. V. Vilnrotter and M Srinivasan, "Adaptive Detector Arrays for Optical Communications Receivers," IEEE Transactions on Communications, Vol. 50, No. 7, July 2002.
6. L. C. Andrews, R. L. Phillips, *Laser Beam Propagation through Random Media*, SPIE Optical Engineering Press, Bellingham, Washington, 1998.
7. P. Negrete-Regagnon, "Practical aspects of image recovery by means of the bispectrum," JOSA, vol.13, no. 7, July 1996.
8. R.A. Oetjen, E.E. Bell, J. Young, L. Eisner, "Spectral radiance of sky and terrain at wavelengths between 1 and 20 microns. I. Instrumentation." JOSA, Vol. 50 Issue 12 Page 1308 (December 1960)
9. J. V. Sandusky, D. J. Hoppe, and M. J. Britcliffe, "Deep-Space Optical Reception Antenna (DSORA): Aperture Versus Quality," TMO PR 42-143, July-September 2000, pp. 1-11, November 15, 2000.